Enhanced thermoelectric perfromance in cubic form of SnSe stabilized through enformatingly alloying AgSbTe$_2$

HPSTAR
1568-2022

Yuping Wang [a], Bingchao Qin [a], Tao Hong [a], Lizhong Su [a], Xiang Gao [b], Dongyang Wang [a],*, Li-Dong Zhao [a],*

[a] School of Materials Science and Engineering, Beihang University, Beijing 100191, China
[b] Center for High Pressure Science and Technology Advanced Research (HPSTAR), Beijing 100094, China

A B S T R A C T

Metastable cubic SnSe has received extensive attention in terms of theoretical predictions since orthorhombic SnSe was experimentally developed as one of the most promising thermoelectric candidates in recent years. In this work, we successfully stabilized the cubic SnSe through AgSbTe$_2$ alloying, after which the thermoelectric transport properties were significantly optimized by simultaneously suppressing lattice and electronic thermal conductivities via introducing Pb. The maximum power factor of (SnSe)$_{0.6}$(AgSbTe$_2$)$_{0.4}$ reached to 13 μWcm^{-1}K^{-2} at 723 K, with a high average power factor of $\sim$ 12 μWcm^{-1}K^{-2} at 300–773 K. Based on 40% AgSbTe$_2$ alloying, the strong phonon-defect scattering and low electronic thermal conductivity caused by Pb alloying contribute greatly to the reduction of total thermal conductivity, while the excellent electrical transport properties were substantially maintained. Finally, the peak *ZT* value reached to 1.20 and a high average *ZT* value of $\sim$ 0.90 over 300–773 K were achieved in the cubic phase (SnSe)$_{0.6}$(AgSbTe$_2$)$_{0.4}$ with 10% Pb alloyed.

© 2022 Acta Materialia Inc. Published by Elsevier Ltd. All rights reserved.

1. Introduction

Since the 20th century, the pace of global modernization has been accelerated, and the rapid industrial development has led to the worse energy crisis. Likewise, fossil fuel combustion caused by environmental pollution has become increasingly serious [1]. Exploring green and renewable energy and technology has been impending. Thermoelectric materials can directly convert heat into electricity and play an important role in waste heat recycling, environmental protection, and sustainable development [2–8]. To expand the utilization of a thermoelectric material, the crucial challenge is to improve its conversion efficiency, the dimensionless figureure of merit, defined as $ZT = S^2\sigma T/(\kappa_{ele}+\kappa_{lat})$, where *S, T, σ,* κ_{ele}, and κ_{lat} are the Seebeck coefficient, absolute temperature, electrical conductivity, electronic thermal conductivity, and lattice thermal conductivity, respectively [2,3,9–12].

The key to optimizing thermoelectric performance is to strike a proper balance among the strongly coupled parameters [1,9,13–17]. Among these parameters, the most famous and intuitive conflicts are between *S, σ*, and κ_{ele}, all of which are significantly related to the carrier concentration (n_H) [18–23], while only κ_{lat} is relatively

independent. Resultantly, reducing κ_{lat} is an effective way to improve thermoelectric performance, which can greatly simplify the optimization process. Therefore, exploring novel materials with intrinsically low thermal conductivity has received extensive attention. SnSe, a nontoxic layered wide-bandgap binary semiconductor in IV-VI metal chalcogenides family [24–30], has aroused the huge interest of researchers due to its ultralow κ_{lat} of 0.23 Wm^{-1}K^{-1} and high *ZT* of 2.6 at 923 K along the crystallographic *b* axis [31]. Since then, much more significant achievements have been accomplished in SnSe thermoelectrics for both crystalline [31–38] and polycrystalline [39–44] forms.

Besides the stable orthorhombic (*Pnma*) phase at low temperatures (*T* < 600 K) and the metastable orthorhombic (*Cmcm*) phase at high temperatures (*T* > 800 K) [31,32,45], theoretical calculations showed that SnSe can also form as a rock-salt cubic structure (*Fm$\bar{3}$m*) at room temperature, which has a small difference in the formation energy compared with the orthorhombic (*Pnma*) phase [46–48]. Unlike *Pnma* and *Cmcm* phases, the rock-salt cubic SnSe can only be stabilized under ultrahigh pressures or through inducing large strains [47,49]. Moreover, the rock-salt cubic SnSe was also predicted to have an ultralow κ_{lat}, which comes from the strong anharmonicity and acoustic phonon mode softens [46,50]. Besides, the multiple electronic bands character in the high symmetry cubic SnSe is especially facilitated for electrical transport. In 1967, Marino et al. firstly reported that the rock-salt cubic SnSe

thin films were synthesized on the NaCl substrate through epitaxial growth method under high pressure [51]. Subsequently, Wang et al. also obtained the rock-salt cubic SnSe thin films grown on Bi_2Se_3 substrate using molecular beam epitaxy [49]. Nevertheless, for real thermoelectric applications, it is imperative to explore a more convenient preparation process and obtain large-size bulk samples. Lately, SnSe-AgSbSe$_2$ and SnSe-AgSbTe$_2$ alloys have been implemented to obtain the rock-salt cubic SnSe through the hot pressing method [52–54]. Whereas the average ZT (ZT_{ave}) acquired from SnSe-AgSbSe$_2$ and SnSe-AgSbTe$_2$ alloys were still unsatisfactory. Entropy engineering is one of the powerful approaches to form good thermoelectric materials, which largely lower the lattice thermal conductivity due to the strong phonon scattering that comes from the severe lattice distortions from the mismatch of ionic mass, size, and bond state [55,56]. Liang et al. reported the sustainable role of strong atomic disorder in suppressing the detrimental phase transition and enhancing the thermoelectric performance in GeTe via AgSnSe$_2$ and Sb co-alloying [57]. Samanta et al. reported $ZT \approx 1.3$ at 467 K and $ZT \approx 1.9$ at 660 K in (GeTe)$_{80}$(AgBiSe$_2$)$_{20}$ and (GeTe)$_{80}$(AgSbSe$_2$)$_{20}$, respectively [58–60]. Jiang et al. reported $ZT \approx 1.8$ at 900 K in high-entropy Pb$_{0.89}$Sb$_{0.012}$Sn$_{0.1}$Se$_{0.5}$Te$_{0.25}$S$_{0.25}$ [55]. And Luo et al. reported a peak thermoelectric figure of merit ZT of 1.14 at 723 K, and a high average ZT of ~1.0 over a wide temperature range of 400–773 K in AgSnSbSe$_{1.5}$Te$_{1.5}$ [53].

In this work, the cubic polycrystalline SnSe is implemented via alloying rock-salt phase AgSbTe$_2$ at ambient temperature and pressure. Alloying AgSbTe$_2$ introduces point defects to strengthen phonon scattering, which is beneficial for lowering lattice thermal conductivity. Based on the ultrahigh carrier concentrations (2–5 × 10^{21} cm^{-3}), the electrical conductivity of SnSe-AgSbTe$_2$ was significantly improved, exhibiting a metallic conduction behavior. Meanwhile, the Seebeck coefficient correspondingly declined from ~ 500 μVK^{-1} for pristine SnSe to ~ 100 μVK^{-1} for AgSbTe$_2$-alloyed samples at 300 K. Resultantly, the optimization of final thermoelectric performance and ZT values can not comparable to expection, which is mainly due to the increase in the total thermal conductivity caused by the enhancement of electronic thermal conductivity. Studies have predicted that the optimal carrier concentration for SnSe-AgSbTe$_2$ system is 1–3 × 10^{20} cm^{-3} [31,32,38,61]. This inspires us to further dedicate the reduction of the carrier concentration. Based on 40% AgSbTe$_2$ alloying, the carrier concentration is reduced by further introducing Pb to suppress the Sn vacancy and reduce the band effective mass, resulting in a minimum carrier concentration of 3.8 × 10^{20} cm^{-3} for 14% Pb alloyed samples. Besides, the thermal conductivity of (Sn$_{1-x}$Pb$_x$Se)$_{0.6}$(AgSbTe$_2$)$_{0.4}$ was significantly suppressed from both the lattice and electronic parts, due to the strain and mass fluctuations induced by Pb alloying, and the decreased carrier concentration, respectively [37]. Collectively, benefiting from the highly maintained electrical transport and obviously decreased thermal conductivity, a peak ZT of ~ 1.20 at 723 K and a high ZT_{ave} of ~ 0.90 between 300 - 773 K were obtained in (Sn$_{0.9}$Pb$_{0.1}$Se)$_{0.6}$(AgSbTe$_2$)$_{0.4}$. Our research reveals that high thermoelectric performance can be experimentally realized in the stabilized cubic-structure SnSe, providing an entirely new understanding of practical application for this environmentally friendly and inexpensive thermoelectric material.

2. Experimental section

The polycrystalline samples used in this work were synthesized by the melting method and densified by spark plasma sintering (SPS-211Lx). The more detailed experimental sections including sample preparation and synthesis conditions, the introduction of thermoelectric measuring instruments, and the experimental char-
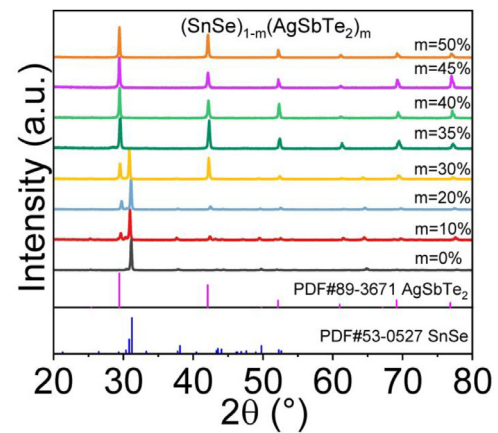

Fig. 1. The room-temperature powder X-ray diffraction (PXRD) patterns of (SnSe)$_{1-m}$(AgSbTe$_2$)$_m$ (m = 0%, 10%, 20%, 30%, 35%, 40%, 45% and 50%) samples.

acterizations can all be found in the Supporting Information (SI). In the following discussions, the measurement direction of the sample is perpendicular to the pressing direction.

3. Results and discussion

3.1. Phase structure characterization

Fig. 1 exhibits the powder X-ray diffraction (PXRD) patterns for the (SnSe)$_{1-m}$(AgSbTe$_2$)$_m$ (m = 0%, 10%, 20%, 30%, 35%, 40%, 45% and 50%) samples. As illustrated in Fig. 1, unalloyed SnSe are well indexed with the low-temperature orthorhombic (Pnma) phase (PDF No. 53–0527). After AgSbTe$_2$ alloying, the samples (m = 10%, 20% and 30%) show as mixed phases. The Bragg peaks belonging to Pnma phase vanished from $m \geq 35\%$, and the samples can be indexed to the high symmetry rock-salt cubic phase with space group $Fm\bar{3}m$ (PDF No. 89–3671). The lattice parameters of the pure phases (alloyed 0% and 35–50% AgSbTe$_2$), as shown in Table S1. As demonstrated, we successfully stabilized the high symmetry rock-salt cubic SnSe at room temperature and ambient pressure through alloying certain contents of AgSbTe$_2$.

3.2. Microstructures of the (SnSe)$_{0.6}$(AgSbTe$_2$)$_{0.4}$ sample

The stabilized phase from orthorhombic to cubic can also be verified by the high-resolution transmission electron microscopy (HRTEM) and the corresponding selected area electron diffraction (SAED) patterns along with the [111] and [100] zone axes in Fig. 2. Fig. 2a and c elucidate that the sample has the same rock-salt ($Fm\bar{3}m$) structure as AgSbTe$_2$. A lattice parameter $a \approx 6.055$ Å was obtained through Rietveld refinement of the room temperature PXRD pattern of the cubic (SnSe)$_{0.6}$(AgSbTe$_2$)$_{0.4}$ sample, while parameters of $a \approx 6.098$ Å and $a \approx 6.079$ Å were calculated by SAED patterns along with the [111] and [100] zone axes respectively, which are well indexed with the standard AgSbTe$_2$ (PDF No. 89–3671). Additionally, the scanning transmission electron microscopy (STEM) and energy-dispersive X-ray spectroscopy (EDS) elemental maps indicate the homogeneous distribution of Sn, Se, Ag, Sb, and Te elements for the sample (SnSe)$_{0.6}$(AgSbTe$_2$)$_{0.4}$, with no second phases detected (Fig. 3). The above microstructure characterizations provide forceful evidence that we successfully realized the stable cubic-structure SnSe in the (SnSe)$_{0.6}$(AgSbTe$_2$)$_{0.4}$ sample.
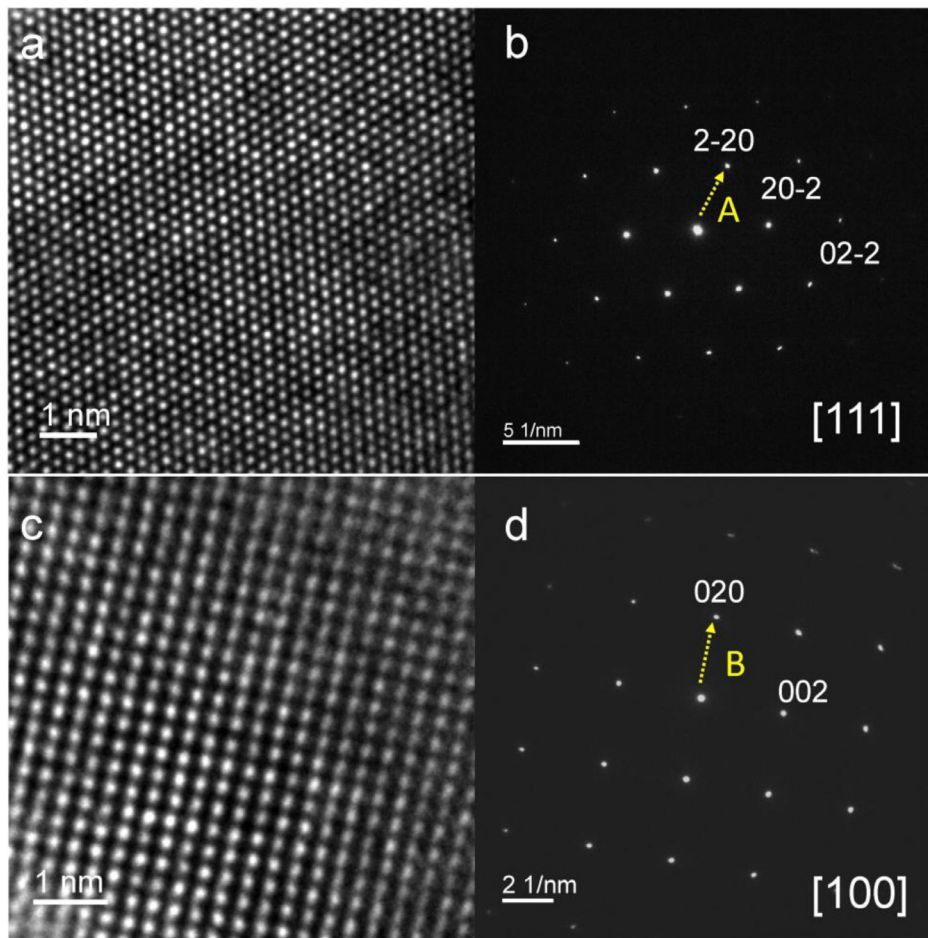
Fig. 2. High-resolution transmission electron microscopy (HRTEM) images ((a) and (c)) and corresponding selected area electron diffraction (SAED) patterns ((b) and (d)) along the [111] and [100] zone axis, respectively.
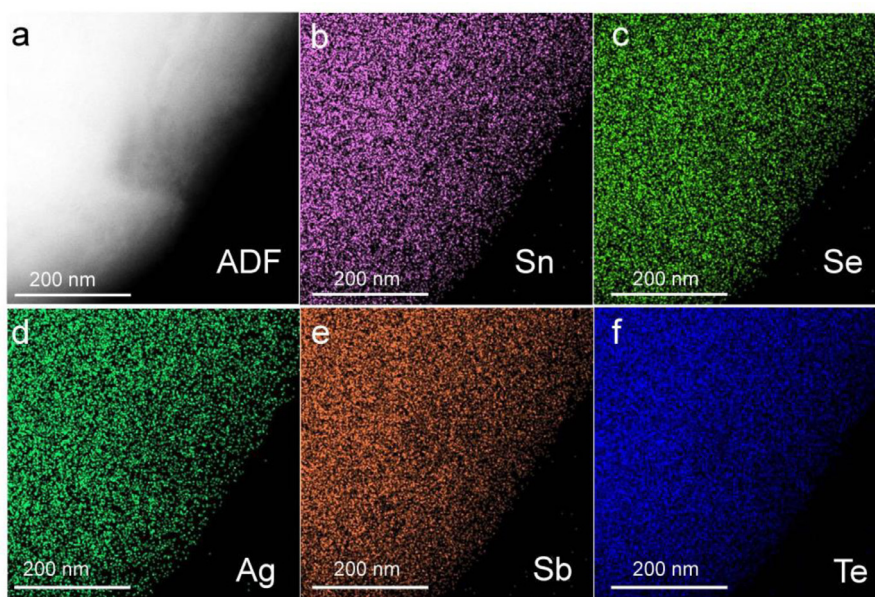

Fig. 3. (a) Annular dark-field scanning transmission electron microscopy (ADF STEM) image of $(SnSe)_{0.6}(AgSbTe_2)_{0.4}$ sample and (b-f) the corresponding elemental mappings obtained from the STEM energy-dispersive X-ray spectroscopy (EDS).
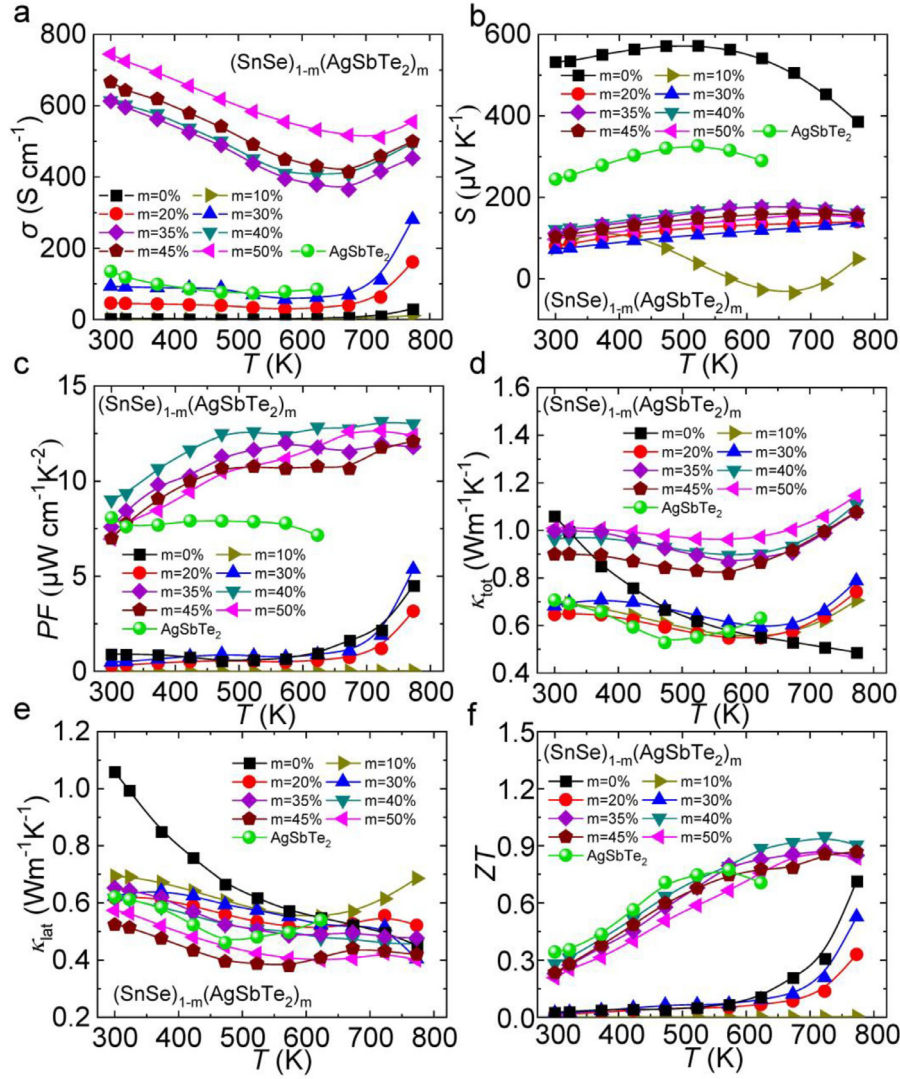
Fig. 4. Temperature-dependent thermoelectric properties for $(SnSe)_{1-m}(AgSbTe_2)_m$ (m = 0%, 10%, 20%, 30%, 35%, 40%, 45%, 50% and 1) samples: (a) Electrical conductivities; (b) Seebeck coefficients; (c) Power factors; (d) Total thermal conductivities; (e) Lattice thermal conductivities; (f) ZT values.

Table 1
The carrier concentration n_H and carrier mobility μ_H at 300 K of the $(SnSe)_{1-m}(AgSbTe_2)_m$ (m = 0%, 10%, 20%, 30%, 35%, 40%, 45% and 50%) samples.

m	0%	10%	20%	30%	35%	40%	45%	50%
n_H (10^{20} cm^{-3})	0.0028	1.24	5.34	8.31	22.0	25.9	27.5	46.1
μ_H (cm^{2}V^{-1}s^{-1})	71.7	0.10	0.54	0.70	1.74	1.48	1.51	1.01

3.3. Thermoelectric properties of $(SnSe)_{1-m}(AgSbTe_2)_m$

The introduction of AgSbTe$_2$ substantially optimized the thermoelectric performance of polycrystalline SnSe. Electrical conductivities with rising temperature for $(SnSe)_{1-m}(AgSbTe_2)_m$ samples are depicted in Fig. 4a. It has been reported that AgSbTe$_2$ alloying can reduce the bandgap and increase the density of state effective mass (m^*) of SnSe, and thus slightly flattened the edge of valence and conduction bands [52]. Compared with the pristine SnSe, the electrical conductivity of the samples has been significantly improved by alloying AgSbTe$_2$, which originates from the sharply increased carrier concentration at room temperature (shown in Table 1) derived from cation vacancies. With small fractions of AgSbTe$_2$ ($m < 35$%) alloyed, the samples exhibit intrinsic semiconducting behavior, and the electrical conductivity grad-

ually increases with rising temperature. With AgSbTe$_2$ fraction increases, the samples show completely different electrical conductivity curves over the whole temperature range. Below $\sim$ 700 K, the electrical conductivity experiences a linearly downward process as temperature increases, showing the metallic conduction behavior, afterwards it goes up at temperatures above 700 K. Upturn of electrical conductivity at high temperatures can be derived from the thermal excitation of minority carriers resulting from bipolar effect. Due to the higher electrical conductivity through activating more hole carriers, the Seebeck coefficient is relatively low over the measured temperature range, as presented in Fig. 4b. Contrary to the trend of electrical conductivity, the Seebeck coefficient decreases at high temperatures. The power factor can be boosted approximately 10 times from $\sim$ 0.9 μWcm^{-1}K^{-2} for pristine SnSe to $\sim$ 9.0 μWcm^{-1}K^{-2} after introducing 40% AgSbTe$_2$

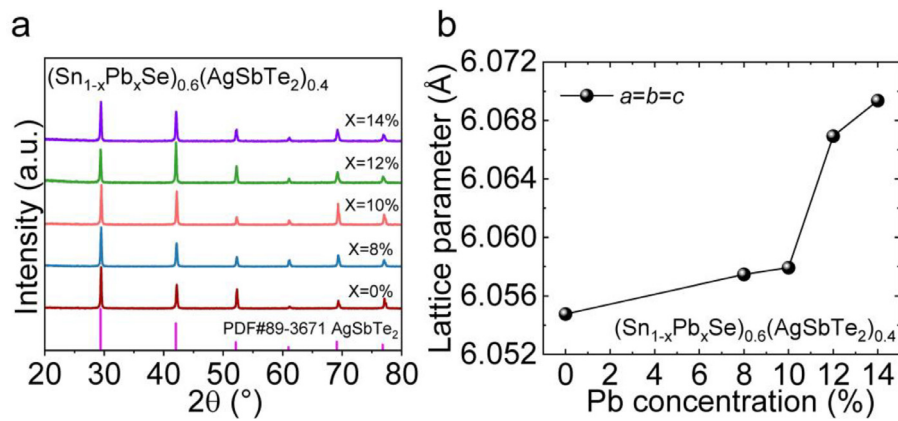**Fig. 5.** (a) PXRD patterns and (b) Lattice parameters of $(Sn_{1-x}Pb_xSe)_{0.6}(AgSbTe_2)_{0.4}$ (x = 0%, 8%, 10%, 12%, and 14%) samples.

at 300 K, as displayed in Fig. 4c, which is originated markedly enhanced electrical conductivities and carrier concentrations. The total thermal conductivities (κ_{tot}) as a function of temperature are shown in Fig. 4d, related parameters including sample density (ρ), specific heat (C_p), thermal diffusivity coefficient (D), electronic thermal conductivity (κ_{ele}), and Lorentz number (L) are displayed in Table S2 and Fig. S1, respectively. The κ_{tot} of rock-salt cubic phase ($m \geq 35\%$) increased significantly with increasing of AgSbTe$_2$-alloyed fraction, while the κ_{lat} declined effectively since the introduction of AgSbTe$_2$ (Fig. 4e), which is due to the establishment of multiple phonon scattering mechanisms incorporating phonon-boundary scattering, phonon-dislocation scattering and phonon-nanoparticle scattering, as already demonstrated before [52]. Thus, the increment of κ_{tot} is mainly contributed from κ_{ele} (Fig. S1c). Fig. 4f depicts the temperature-dependent ZT values for $(SnSe)_{1-m}(AgSbTe_2)_m$ samples. The $(SnSe)_{0.6}(AgSbTe_2)_{0.4}$ sample exhibits a maximum ZT (ZT_{max}) of 0.94 at 723 K, and the average ZT (ZT_{ave}) reaches 0.69 in the temperature region of 300 - 773 K, which is nearly 6 times higher than that of pristine SnSe ($ZT_{ave} \sim$ 0.13 between 300 K and 773 K).

3.4. Phase structure characterization of $(Sn_{1-x}Pb_xSe)_{0.6}(AgSbTe_2)_{0.4}$

As discussed above, the lattice thermal conductivity is relatively high and a further reduction of κ_{lat} is performed by using Pb alloying to introduce the point defect scattering based on the optimized $(SnSe)_{0.6}(AgSbTe_2)_{0.4}$. Fig. 5a demonstrates the PXRD patterns of $(Sn_{1-x}Pb_xSe)_{0.6}(AgSbTe_2)_{0.4}$ (x = 0%, 8%, 10%, 12%, and 14%) samples, indicating that we acquired a hexatomic single-phase with the rock-salt cubic structure system without any impurity phases. The lattice parameters increased with the rising content of Pb, which is caused by the larger ionic radius of Pb^{2+} (1.19 Å) compared to Sn^{2+} (0.87 Å), as depicted in Fig. 5b.

3.5. Thermal transport properties of $(Sn_{1-x}Pb_xSe)_{0.6}(AgSbTe_2)_{0.4}$

Introducing Pb can effectively reduce the total thermal conductivity and the thermal diffusivity over the entire temperature range, as shown in Fig. 6a and b. The relevant parameters to determine κ_{tot} can be found in Fig. S2 and Table S3. An extremely low κ_{tot} of $\sim$ 0.6 Wm^{-1}K^{-1} is achieved in the 14% Pb-alloyed sample at 300 K, originating from the significant reduction of κ_{lat} (Fig. 6c) and κ_{ele} (Fig. 6d), respectively. The increment of κ_{tot} can be found at high temperature, which is resulting from the bipolar effect of carrier displayed in Fig. 6d. To further reveal the mechanism of the reduction in κ_{lat}, the crystal structure of the Pb-alloyed SnSe-AgSbTe$_2$ and octahedral coordination of different

atoms in the lattice was investigated based on the special quasi-random structure, depicted in Fig. S3 and Fig. 7 respectively. As illustrated in Fig. S3, Pb alloying causes strong hierarchical bonding structures in the whole lattice. Obvious off-centering atoms and distorted octahedrons lead to consequent local bonding heterogeneity between the atoms due to Pb allying, as shown in Fig. 7, which increases the anharmonicity of the lattice [62]. Meanwhile, the fluctuations in mass and strain fields are induced by Pb alloying [37]. All of the above mentioned mechanisms will enhance the phonon scattering and hinder the phonon transport, which is crucial for the decline of lattice thermal conductivity. Specifically, the κ_{lat} at 300 K demonstrates an approximately 30% reduction from $\sim$ 0.61 Wm^{-1}K^{-1} for $(SnSe)_{0.6}(AgSbTe_2)_{0.4}$ to $\sim$ 0.43 Wm^{-1}K^{-1} for $(Sn_{0.9}Pb_{0.1}Se)_{0.6}(AgSbTe_2)_{0.4}$, as shown in Fig. 6c. Furthermore, a minimum $\kappa_{lat} \sim$ 0.31 Wm^{-1}K^{-1} at 773 K was achieved, which is an extremely low value compared with other cubic-structure promising thermoelectrics [63–68]. The κ_{ele} depicted in Fig. 6d follows the same trend as κ_{tot}, meanwhile, it has a nearly 55% decrease from $\sim$ 0.35 Wm^{-1}K^{-1} to $\sim$ 0.16 Wm^{-1}K^{-1} at 300 K. The decrease in κ_{ele} is mainly derived from the reduction of electrical conductivity by Pb-alloying, which will be discussed comprehensively in the following part.

3.6. Electrical transport properties of $(Sn_{1-x}Pb_xSe)_{0.6}(AgSbTe_2)_{0.4}$

Fig. 8 depicts the electrical performance of Pb alloyed samples. Fig. 8a exhibits the electrical conductivities of $(Sn_{1-x}Pb_xSe)_{0.6}(AgSbTe_2)_{0.4}$ (x = 0%, 8%, 10%, 12%, and 14%) samples with increasing temperature. Due to the decreased Sn vacancies (V_{Sn}) by the introduction of Pb [37,69], the electrical conductivities distinctly declined from $\sim$ 614 S cm^{-1} (x = 0%) to $\sim$ 330 S cm^{-1} (x = 14%) at 300 K. The decrease in electrical conductivities directly causes the reduction of κ_{ele} over the whole temperature range, as demonstrated in Fig. 6d. Specifically, the carrier concentration (n_H) at 300 K decreases from $\sim$ 2.6 × 10^{21} cm^{-3} for $(SnSe)_{0.6}(AgSbTe_2)_{0.4}$ to $\sim$ 3.8 × 10^{20} cm^{-3} for $(Sn_{0.86}Pb_{0.14}Se)_{0.6}(AgSbTe_2)_{0.4}$, while the carrier mobility (μ_H) significantly improved because of the decreased carrier concentration as well as the suppressed Sn vacancies induced by Pb alloying, as clearly shown in Fig. 8b. The decreased n_H significantly optimize the Seebeck coefficients over the entire temperature range (Fig. 8c). The inflections of the electrical conductivity and Seebeck coefficient at high temperatures can be attributed to the bipolar effect. As Fig. 8d demonstrates, the experimental carrier mobility is located above the theoretical line for $(SnSe)_{0.6}(AgSbTe_2)_{0.4}$ (black solid line) from the single band model, which indicates that the increase of carrier mobility not only arises from the loss of carrier concentration but also the suppression of scattering
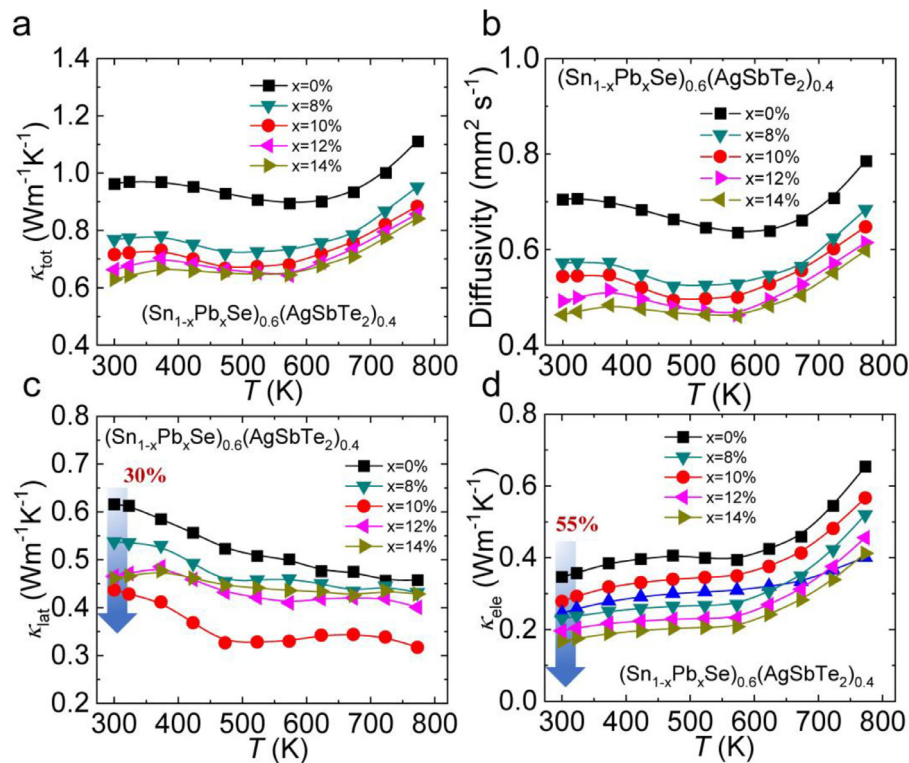
Fig. 6. Temperature-dependent thermal properties for $(Sn_{1-x}Pb_xSe)_{0.6}(AgSbTe_2)_{0.4}$ ($x = 0\%$, 8%, 10%, 12%, and 14%) samples: (a) Total thermal conductivities; (b) Thermal diffusivity coefficient; (c) Lattice thermal conductivities; (d) Electronic thermal conductivities.
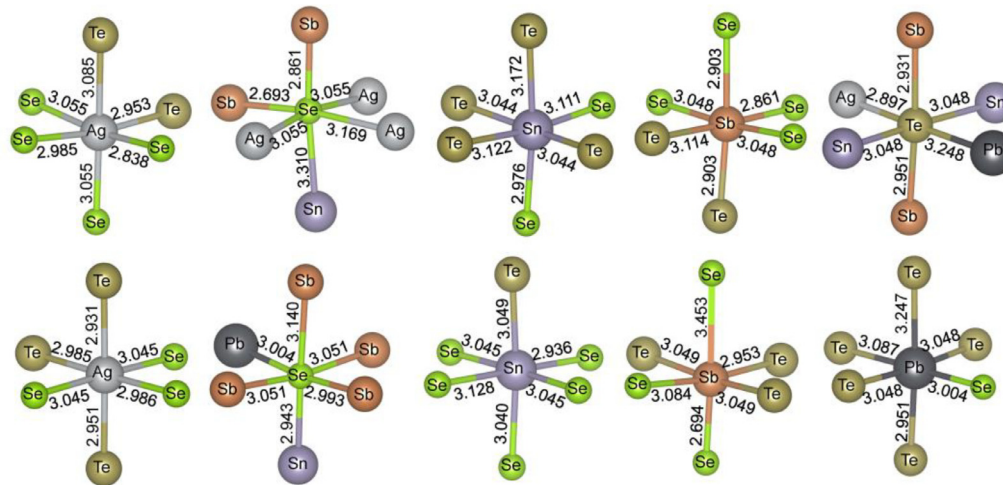

Fig. 7. Distorted octahedral coordination around different center atoms in $Sn_7PbAg_4Sb_4Se_8Te_8$ at room temperature.

between carrier and vacancy defects. The blue dotted line for p-type polycrystalline $Pnma$-SnSe was plotted for comparison. Similarly, the Pisarenko lines calculated by the single band model at 300 K with different effective mass ($m^* = 0.8m_0$ and $12.05m_0$) and experimental Seebeck coefficients are depicted in Fig. 8e. The experimental data for Pb-alloyed samples was located between the black solid line and blue dotted line. While m^* is still much higher than that of $Pnma$-SnSe, Pb alloying significantly lowers the band effective mass m^* of cubic $(SnSe)_{0.6}(AgSbTe_2)_{0.4}$. To further investigate the effects on the Seebeck coefficient from Pb alloying, we conducted first-principal calculations of the electronic density of state (DOS) for $(SnSe)_{0.667}(AgSbTe_2)_{0.333}$ with and without Pb

alloying, as shown in Fig. S4a. Compared with the Pb-free sample, it is found that introducing Pb can make the DOS curves more complanate near the Fermi level, thereby reducing the effective mass. The relatively smaller band effective mass m^* can give rise to higher carrier mobility since the relationship $\mu_H = e\tau/m^*$ (e is the charge of electron, τ is the relaxation time). As the result, the optimized carrier mobility originates from both the obvious diminution on carrier concentration and the reduction on band effective mass. The Pb-alloyed $(SnSe)_{0.6}(AgSbTe_2)_{0.4}$ exhibits slightly lower electrical conductivity but significantly higher Seebeck coefficient, leading to the maintained high power factors over a wide temperature range, as depicted in Fig. 8f.
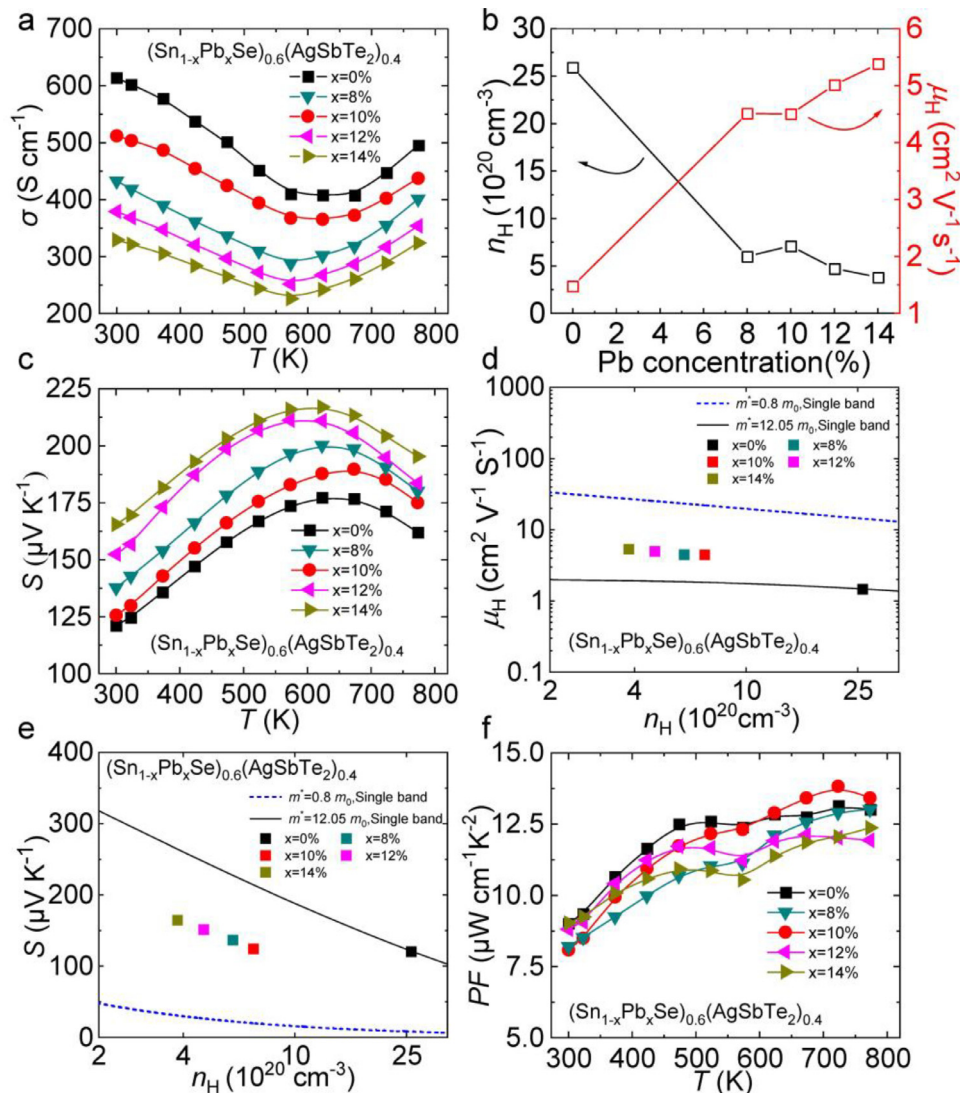
Fig. 8. Electrical transport properties for $(Sn_{1-x}Pb_xSe)_{0.6}(AgSbTe_2)_{0.4}$ (x = 0%, 8%, 10%, 12%, and 14%) samples as a function of temperature (a) Electrical conductivities; (b) Carrier concentration and carrier mobility at 300 K; (c) Seebeck coefficients; (d) Carrier mobility as a function of carrier concentration; (e) Pisarenko plots of $(Sn_{1-x}Pb_xSe)_{0.6}(AgSbTe_2)_{0.4}$ with different m^* and experimental data at 300 K; (f) Power factors.
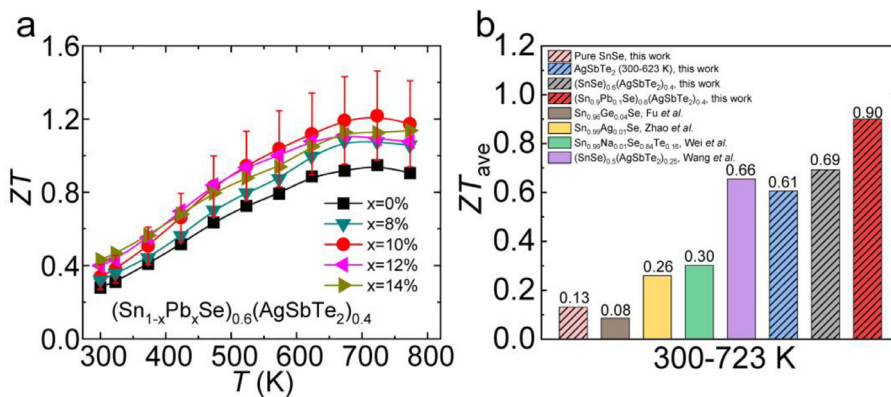

Fig. 9. (a) Temperature-dependent ZT values for $(Sn_{1-x}Pb_xSe)_{0.6}(AgSbTe_2)_{0.4}$ (x = 0%, 8%, 10%, 12%, and 14%) samples; (b) ZT_{ave} of this work and other p-type polycrystalline SnSe systems at 300 - 773 K[40,52,70,71] and printine $AgSbTe_2$ at 300 - 623 K.

3.7. ZT values and remarkable average ZT (ZT$_{ave}$) for $(Sn_{1-x}Pb_xSe)_{0.6}(AgSbTe_2)_{0.4}$

The temperature-dependent dimensionless *ZT* values of $(Sn_{1-x}Pb_xSe)_{0.6}(AgSbTe_2)_{0.4}$ (*x* = 0%, 8%, 10%, 12%, and 14%) samples demonstrated in Fig. 9a. Limited by the high total thermal conductivity, the maximum *ZT* (*ZT*$_{max}$) of $(SnSe)_{0.6}(AgSbTe_2)_{0.4}$ only reaches ~ 0.94 at 723 K. Pb alloying contributes greatly to the decreased total thermal conductivity while having no harmful effect on the electrical transports, leading to much higher *ZT* and *ZT*$_{ave}$ in the measurement temperature range. Specifically, a peak *ZT* ~ 1.20 is achieved by alloying 10% Pb in $(SnSe)_{0.6}(AgSbTe_2)_{0.4}$ system, with a high *ZT*$_{ave}$ approaching ~ 0.90. For thermoelectric materials, *ZT*$_{max}$ and *ZT*$_{ave}$ are both essential for higher energy conversion efficiency. The $(Sn_{0.9}Pb_{0.1}Se)_{0.6}(AgSbTe_2)_{0.4}$ sample obtained in this study demonstrates comparable *ZT*$_{max}$ but much higher *ZT*$_{ave}$ at 300-773 K compared with the previously reported *p*-type polycrystalline SnSe systems [40,52,70,71], as depicted in Fig. 9b. The Pb alloying optimize visibly *ZT*$_{ave}$ due to the simultaneous suppression on both lattice and electronic thermal conductivities. The *ZT*$_{ave}$ of ~ 0.90 rivals those of other *p*-type polycrystalline SnSe systems as well as the pristine AgSbTe$_2$. The energy conversion efficiency (η) can be calculated based on the *ZT*$_{ave}$ by the following formula [32]:

$$\eta = \frac{T_h - T_c}{T_h} \times \frac{\sqrt{1 + ZT_{ave}} - 1}{\sqrt{1 + ZT_{ave}} + T_c/T_h} \tag{1}$$

where T_h represents the hot side temperature, T_c represents cold side temperature. The projected conversion efficiency of the 10% Pb alloyed sample exceeds 13% at a temperature difference of 473 K, which is much higher than other *p*-type polycrystalline SnSe systems (Fig. S5).

4. Conclusions

In this work, we successfully realized the stable cubic-structure SnSe-based bulk samples by alloying AgSbTe$_2$ using the melting and SPS method. Alloying AgSbTe$_2$ can significantly optimize the electrical transport properties of the cubic SnSe. The maximum average power factor reaches ~ 12 μWcm^{-1}K^{-2} for $(SnSe)_{0.6}(AgSbTe_2)_{0.4}$, which is 10 times higher than that of pristine SnSe (300–773 K). Pb alloying on Sn sites can further suppress the thermal transport, which can resultantly reduce both the lattice thermal conductivity by inducing mass and strain field fluctuations and electronic thermal conductivity due to the significant reduction in hole carrier concentration. Moreover, Pb alloying retains relatively high electrical transport properties besides the prominent reduction in thermal conductivity. Resultantly, the 10% Pb-alloyed sample demonstrates the final *ZT*$_{max}$ and *ZT*$_{ave}$ values approaching ~ 1.20 and 0.90, respectively. Present results confirm that the cubic-structure SnSe shows desirable thermoelectric performance compared to orthorhombic SnSe, and will broaden the applications for SnSe-based thermoelectrics in the field of waste heat recovery.

Declaration of Competing Interest

The authors declare that they have no known competing financial interests or personal relationships that could have appeared to influence the work reported in this paper.

Acknowledgments

Supplementary materials

Supplementary material associated with this article can be found, in the online version, at doi:10.1016/j.actamat.2022.117681.

References

[1] X.L. Shi, J. Zou, Z.G. Chen, Advanced thermoelectric design: from materials and structures to devices, Chem. Rev. 120 (15) (2020) 7399–7515.

[2] G.J. Snyder, E.S. Toberer, Complex thermoelectric materials, Nat. Mater. 7 (2) (2008) 105–114.

[3] J.R. Sootsman, D.Y. Chung, M.G. Kanatzidis, New and old concepts in thermoelectric materials, Angew. Chem. Int. Ed. Engl. 48 (46) (2009) 8616–8639.

[4] D. Wu, Y. Pei, Z. Wang, H. Wu, L. Huang, L.D. Zhao, J. He, Significantly enhanced thermoelectric performance in N-type heterogeneous BiAgSeS composites, Adv. Funct. Mater. 24 (48) (2014) 7763–7771.

[5] X. Liu, D. Wang, H. Wu, J. Wang, Y. Zhang, G. Wang, S.J. Pennycook, L.D. Zhao, Intrinsically low thermal conductivity in BiSbSe$_3$: a promising thermoelectric material with multiple conduction bands, Adv. Funct. Mater. 29 (3) (2019) 1806558.

[6] Z. Zhang, K. Zhao, T.R. Wei, P. Qiu, L. Chen, X. Shi, Cu$_2$Se-based liquid-like thermoelectric materials: looking back and stepping forward, Energy Environ. Sci. 13 (10) (2020) 3307–3329.

[7] Z. Gao, Q. Yang, P. Qiu, T.R. Wei, S. Yang, J. Xiao, L. Chen, X. Shi, P-type plastic inorganic thermoelectric materials, Adv. Energy Mater. 11 (23) (2021) 2100883.

[8] X. Shi, J. He, Thermopower and harvesting heat, Science 371 (6527) (2021) 343–344.

[9] G. Tan, L.D. Zhao, M.G. Kanatzidis, Rationally designing high-performance bulk thermoelectric materials, Chem. Rev. 116 (19) (2016) 12123–12149.

[10] X. Zhang, L.D. Zhao, Thermoelectric materials: energy conversion between heat and electricity, J. Materiomics 1 (2) (2015) 92–105.

[11] X. Qian, H. Wu, D. Wang, Y. Zhang, J. Wang, G. Wang, L. Zheng, S.J. Pennycook, L.D. Zhao, Synergistically optimizing interdependent thermoelectric parameters of N-type PbSe through alloying CdSe, Energy Environ. Sci. 12 (6) (2019) 1969–1978.

[12] K.P. Zhao, E. Eikeland, D.S. He, W.J. Qiu, Z.C. Jin, Q.F. Song, T.R. Wei, P.F. Qiu, J.J. Liu, J.Q. He, B.B. Iversen, J. He, L.D. Chen, X. Shi, Thermoelectric materials with crystal-amorphicity duality induced by large atomic size mismatch, Joule 5 (5) (2021) 1183–1195.

[13] B.C. Qin, Y. Xiao, Y.M. Zhou, L.D. Zhao, Thermoelectric transport properties of Pb-Sn-Te-Se system, Rare Met. 37 (4) (2018) 343–350.

[14] B.C. Qin, X.G. Hu, Y. Zhang, H.J. Wu, S.J. Pennycook, L.D. Zhao, Comprehensive investigation on the thermoelectric properties of P-type PbTe-PbSe-PbS alloys, Adv. Electron. Mater. 5 (12) (2019) 1900609.

[15] B.C. Qin, D.Y. Wang, L.D. Zhao, Slowing down the heat in thermoelectrics, InfoMat 3 (7) (2021) 755–789.

[16] W. He, D. Wang, J.F. Dong, Y. Qiu, L. Fu, Y. Feng, Y. Hao, G. Wang, J. Wang, C. Liu, J.F. Li, J. He, L.D. Zhao, Remarkable electron and phonon band structures lead to a high thermoelectric performance ZT >1 in earth-abundant and eco-friendly SnS crystals, J. Mater. Chem. A 6 (21) (2018) 10048–10056.

[17] W.W. Qu, X.X. Zhang, B.F. Yuan, L.D. Zhao, Homologous layered InFeO$_3$(ZnO)$_{(m)}$: new promising abradable seal coating materials, Rare Met. 37 (2) (2018) 79–94.

[18] Z. Chen, X. Zhang, Y. Pei, Manipulation of phonon transport in thermoelectrics, Adv. Mater. 30 (17) (2018) 1705617.

[19] S. Hui, W.P. Gao, X. Lu, A. Panda, T.P. Bailey, A.A. Page, S.R. Forrest, D.T. Morelli, X.Q. Pan, K.P. Pipe, C. Uher, Engineering temperature-dependent carrier concentration in bulk composite materials via temperature-dependent Fermi level offset, Adv. Energy Mater. 8 (3) (2018) 1701623.

[20] T. Zhu, Y. Liu, C. Fu, J.P. Heremans, J.G. Snyder, X. Zhao, Compromise and synergy in high-efficiency thermoelectric materials, Adv. Mater. 29 (14) (2017) 1605884.

[21] Y.L. Pei, H. Wu, J. Sui, J. Li, D. Berardan, C. Barreteau, L. Pan, N. Dragoe, W.S. Liu, J. He, L.D. Zhao, High thermoelectric performance in N-type BiAgSeS due to intrinsically low thermal conductivity, Energy Environ. Sci. 6 (6) (2013) 1750–1755.

[22] X. Zhang, C. Chang, Y. Zhou, L.D. Zhao, BiCuSeO thermoelectrics: an update on recent progress and perspective, Materials 10 (2) (2017) 198 (Basel).

[23] Y. Xiao, D. Wang, B. Qin, J. Wang, G. Wang, L.D. Zhao, Approaching topological insulating states leads to high thermoelectric performance in N-type PbTe, J. Am. Chem. Soc. 140 (40) (2018) 13097–13102.

[24] Y.K. Lee, Z. Luo, S.P. Cho, M.G. Kanatzidis, I. Chung, Surface oxide removal for polycrystalline SnSe reveals near-single-crystal thermoelectric performance, Joule 3 (3) (2019) 719–731.

[25] A.T. Duong, V.Q. Nguyen, G. Duvjir, V.T. Duong, S. Kwon, J.Y. Song, J.K. Lee, J.E. Lee, S. Park, T. Min, J. Lee, J. Kim, S. Cho, Achieving ZT = 2.2 with Bi-doped N-type SnSe single crystals, Nat. Commun. 7 (2016) 13713.

[26] S. Chandra, K. Biswas, Realization of high thermoelectric figure of merit in solution synthesized 2D SnSe nanoplates via Ge alloying, J. Am. Chem. Soc. 141 (15) (2019) 6141–6145.

[27] W. Wei, C. Chang, T. Yang, J. Liu, H. Tang, J. Zhang, Y. Li, F. Xu, Z. Zhang, J.F. Li, G. Tang, Achieving high thermoelectric figure of merit in polycrystalline SnSe via introducing Sn vacancies, J. Am. Chem. Soc. 140 (1) (2018) 499–505.

[28] J. Liu, P. Wang, M.Y. Wang, R. Xu, J. Zhang, J.Z. Liu, D. Li, N.N. Liang, Y.W. Du, G. Chen, G.D. Tang, Achieving high thermoelectric performance with Pb and Zn codoped polycrystalline SnSe via phase separation and nanostructuring strategies, Nano Energy 53 (2018) 683–689.

[29] G. Tang, W. Wei, J. Zhang, Y. Li, X. Wang, G. Xu, C. Chang, Z. Wang, Y. Du, L.D. Zhao, Realizing high figure of merit in phase-separated polycrystalline $Sn_{1-x}Pb_xSe$, J. Am. Chem. Soc. 138 (41) (2016) 13647–13654.

[30] C. Chang, G. Tan, J. He, M.G. Kanatzidis, L.D. Zhao, The thermoelectric properties of SnSe continue to surprise: extraordinary electron and phonon transport, Chem. Mater. 30 (21) (2018) 7355–7367.

[31] L.D. Zhao, S.H. Lo, Y. Zhang, H. Sun, G. Tan, C. Uher, C. Wolverton, V.P. Dravid, M.G. Kanatzidis, Ultralow thermal conductivity and high thermoelectric figure of merit in SnSe crystals, Nature 508 (7496) (2014) 373–377.

[32] L.D. Zhao, G. Tan, S. Hao, J. He, Y. Pei, H. Chi, H. Wang, S. Gong, H. Xu, V.P. Dravid, C. Uher, G.J. Snyder, C. Wolverton, M.G. Kanatzidis, Ultrahigh power factor and thermoelectric performance in hole-doped single-crystal SnSe, Science 351 (6269) (2016) 141–144.

[33] B.C. Qin, Y. Zhang, D.Y. Wang, Q. Zhao, B.C. Gu, H.J. Wu, H.J. Zhang, B.J. Ye, S.J. Pennycook, L.D. Zhao, Ultrahigh average *ZT* realized in P-type SnSe crystalline thermoelectrics through producing extrinsic vacancies, J. Am. Chem. Soc. 142 (12) (2020) 5901–5909.

[34] B.C. Qin, D.Y. Wang, W.K. He, Y. Zhang, H.J. Wu, S.J. Pennycook, L.D. Zhao, Realizing high thermoelectric performance in P-type SnSe through crystal structure modification, J. Am. Chem. Soc. 141 (2) (2019) 1141–1149.

[35] B.C. Qin, W.K. He, L.D. Zhao, Estimation of the potential performance in P-type SnSe crystals through evaluating weighted mobility and effective mass, J. Materiomics 6 (4) (2020) 671–676.

[36] B.C. Qin, D.Y. Wang, X.X. Liu, Y.X. Qin, J.F. Dong, J.F. Luo, J.W. Li, W. Liu, G.J. Tan, X.F. Tang, J.F. Li, J.Q. He, L.D. Zhao, Power generation and thermoelectric cooling enabled by momentum and energy multiband alignments, Science 373 (6554) (2021) 556–561.

[37] C. Chang, D.Y. Wang, D.S. He, W.K. He, F.Y. Zhu, G.T. Wang, J.Q. He, L.D. Zhao, Realizing high-ranged out-of-plane *ZT*s in N-type SnSe crystals through promoting continuous phase transition, Adv. Energy Mater. 9 (28) (2019) 1901334.

[38] C. Chang, M. Wu, D. He, Y. Pei, C.F. Wu, X. Wu, H. Yu, F. Zhu, K. Wang, Y. Chen, L. Huang, J.F. Li, J. He, L.D. Zhao, 3D charge and 2D phonon transports leading to high out-of-plane *ZT* in N-type SnSe crystals, Science 360 (6390) (2018) 778–783.

[39] Q. Zhao, D. Wang, B. Qin, G. Wang, Y. Qiu, L.D. Zhao, Synergistically optimized electrical and thermal transport properties of polycrystalline SnSe via alloying SnS, J. Solid State Chem. 273 (2019) 85–91.

[40] Q. Zhao, B. Qin, D. Wang, Y. Qiu, L.D. Zhao, Realizing high thermoelectric performance in polycrystalline SnSe via silver doping and germanium alloying, ACS Appl. Energy Mater. 3 (3) (2019) 2049–2054.

[41] J. Liu, P. Wang, M. Wang, R. Xu, G. Tang, Achieving high thermoelectric performance with Pb and Zn codoped polycrystalline SnSe via phase separation and nanostructuring strategies, Nano Energy 53 (2018) 683–689.

[42] Z.H. Ge, D. Song, X. Chong, F. Zheng, L. Jin, X. Qian, L. Zheng, R.E. Dunin-Borkowski, P. Qin, J. Feng, L.D. Zhao, Boosting the thermoelectric performance of (Na,K)-codoped polycrystalline SnSe by synergistic tailoring of the band structure and atomic-scale defect phonon scattering, J. Am. Chem. Soc. 139 (28) (2017) 9714–9720.

[43] S. Gowthamaraju, U.P. Deshpande, P.A. Bhobe, Augmentation of the thermoelectric properties of polycrystalline tin selenides via formation of $SnSe/SnSe_2$ composites, J. Mater. Sci. Mater. Electron. 32 (9) (2021) 11781–11790.

[44] S. Li, X.N. Lou, X.T. Li, J. Zhang, D. Li, H.Q. Deng, J.Z. Liu, G.D. Tang, Realization of high thermoelectric performance in polycrystalline tin selenide through schottky vacancies and endotaxial nanostructuring, Chem. Mater. 32 (22) (2020) 9761–9770.

[45] L.D. Zhao, C. Chang, G.J. Tan, M.G. Kanatzidis, SnSe: a remarkable new thermoelectric material, Energy Environ. Sci. 9 (10) (2016) 3044–3060.

[46] D.Y. Wang, W.K. He, C. Chang, G.T. Wang, J.F. Wang, L.D. Zhao, Thermoelectric transport properties of rock-salt SnSe: first-principles investigation, J. Mater. Chem. C 6 (44) (2018) 12016–12022.

[47] Y. Sun, Z.C. Zhong, T. Shirakawa, C. Franchini, D.Z. Li, Y.Y. Li, S. Yunoki, X.Q. Chen, Rocksalt SnS and SnSe: native topological crystalline insulators, Phys. Rev. B 88 (23) (2013) 235122.

[48] S.U. Rehman, F.K. Butt, Z. Tariq, F. Hayat, R. Gilani, F. Aleem, Pressure induced structural and optical properties of cubic phase SnSe: an investigation for the infrared/mid-infrared optoelectronic devices, J. Alloys Compd. 695 (2017) 194–201.

[49] Z. Wang, J. Wang, Y. Zang, Q. Zhang, J.A. Shi, T. Jiang, Y. Gong, C.L. Song, S.H. Ji, L.L. Wang, L. Gu, K. He, W. Duan, X. Ma, X. Chen, Q.K. Xue, Molecular beam epitaxy-grown SnSe in the rock-salt structure: an artificial topological crystalline insulator material, Adv. Mater. 27 (28) (2015) 4150–4154.

[50] Y. Xie, Y. Zhou, X.G. Gong, The intrinsic low lattice thermal conductivity in the rock salt SnSe, Comput. Mater. Sci. 148 (2018) 54–59.

[51] A.N. Mariano, K.L. Chopra, Polymorphism in some IV-VI compounds induced by high pressure and thin-film epitaxial growth, Appl. Phys. Lett. 10 (10) (1967) 282–284.

[52] H.X. Wang, H.Y. Hu, N. Man, C.L. Xiong, Y.K. Xiao, X.J. Tan, G.Q. Liu, J. Jiang, Band flattening and phonon-defect scattering in cubic $SnSe-AgSbTe_2$ alloy for thermoelectric enhancement, Mater. Today Phys. 16 (2021) 100298.

[53] Y. Luo, S. Hao, S. Cai, T.J. Slade, Z.Z. Luo, V.P. Dravid, C. Wolverton, Q. Yan, M.G. Kanatzidis, High thermoelectric performance in the new cubic semiconductor $AgSnSbSe_3$ by high-entropy engineering, J. Am. Chem. Soc. 142 (35) (2020) 15187–15198.

[54] H.X. Wang, L.S. Mao, X.J. Tan, G.Q. Liu, J.T. Xu, H.Z. Shao, H.Y. Hu, J. Jiang, Nontrivial thermoelectric behavior in cubic SnSe driven by spin-orbit coupling, Nano Energy 51 (2018) 649–655.

[55] B. Jiang, Y. Yu, J. Cui, X. Liu, L. Xie, J. Liao, Q. Zhang, Y. Huang, S. Ning, B. Jia, B. Zhu, S. Bai, J. He, High-entropy-stabilized chalcogenides with high thermoelectric performance, Science 371 (2021) 830–834.

[56] Y. Qiu, Y. Jin, D. Wang, M. Guan, W. He, S. Peng, R. Liu, X. Gao, L.D. Zhao, Realizing high thermoelectric performance in GeTe through decreasing the phase transition temperature via entropy engineering, J. Mater. Chem. A 7 (46) (2019) 26393–26401.

[57] G. Liang, T. Lyu, L. Hu, W. Qu, S. Zhi, J. Li, Y. Zhang, J. He, J. Li, F. Liu, C. Zhang, W. Ao, H. Xie, H. Wu, $GeTe_{1-x}(AgSnSe_2)_x$: strong atomic disorder-induced high thermoelectric performance near the Ioffe-Regel limit, ACS Appl. Mater. Interfaces 13 (39) (2021) 47081–47089.

[58] M. Samanta, S. Roychowdhury, J. Ghatak, S. Perumal, K. Biswas, Ultrahigh average thermoelectric figure of merit, low lattice thermal conductivity and enhanced microhardness in nanostructured $(GeTe)_x(AgSbSe_2)_{100-x}$, Chem. Eur. J. 23 (2017) 7438–7443.

[59] M. Samanta, T. Ghosh, R. Arora, U.V. Waghmare, K. Biswas, Realization of both N- and P-type GeTe thermoelectrics: electronic structure modulation by $AgBiSe_2$ alloying, J. Am. Chem. Soc. 141 (49) (2019) 19505–19512.

[60] Z. Zhang, K. Zhao, H. Chen, Q. Ren, Z. Yue, T.R. Wei, P. Qiu, L. Chen, X. Shi, Entropy engineering induced exceptional thermoelectric and mechanical performances in $Cu_{2-y}Ag_yTe_{1-2x}S_xSe_x$, Acta Mater. 224 (2022).

[61] L.S. Mao, Y.N. Yin, Q. Zhang, G.Q. Liu, H.X. Wang, Z. Guo, H.Y. Hu, Y.K. Xiao, X.J. Tan, J. Jiang, Fermi-surface dynamics and high thermoelectric performance along the out-of-plane direction in N-type SnSe crystals, Energy Environ. Sci. 13 (2) (2020) 616–621.

[62] M. Dutta, K. Pal, M. Etter, U.V. Waghmare, K. Biswas, Emphanisis in cubic $(SnSe)_{0.5}(AgSbSe_2)_{0.5}$: dynamical off-centering of anion leads to low thermal conductivity and high thermoelectric performance, J. Am. Chem. Soc. 143 (40) (2021) 16839–16848.

[63] X. Qian, Y. Xiao, C. Chang, L. Zheng, L.D. Zhao, Synergistically optimizing electrical and thermal transport properties of N-type PbSe, Prog. Nat. Sci. Mater. 28 (3) (2018) 275–280.

[64] Y. Qin, D. Wang, Z. Hou, Y. Xiao, G. Wang, Z. Huang, L.D. Zhao, Thermoelectric transport properties of PbS and its contrasting electronic band structures, Scr. Mater. 185 (2020) 76–81.

[65] Y.X. Qin, Y. Xiao, D.Y. Wang, B.C. Qin, Z.W. Huang, L.D. Zhao, An approach of enhancing thermoelectric performance for P-type PbS: decreasing electronic thermal conductivity, J. Alloys Compd. 820 (2020) 153453.

[66] Y. Xiao, D. Wang, Y. Zhang, C. Chen, S. Zhang, K. Wang, G. Wang, S.J. Pennycook, G.J. Snyder, H. Wu, L.D. Zhao, Band sharpening and band alignment enable high quality factor to enhance thermoelectric performance in N-type PbS, J. Am. Chem. Soc. 142 (8) (2020) 4051–4060.

[67] Z. Hou, D. Wang, T. Hong, Y. Qin, S. Peng, G. Wang, J. Wang, X. Gao, Z. Huang, L.D. Zhao, Boosting thermoelectric performance of N-type PbS through synergistically integrating in resonant level and Cu dynamic doping, J. Phys. Chem. Solids 148 (2021) 109640.

[68] Y.X. Qin, T. Hong, B.C. Qin, D.Y. Wang, W.K. He, X. Gao, Y. Xiao, L.D. Zhao, Contrasting Cu roles lead to high ranged thermoelectric performance of PbS, Adv. Funct. Mater. 31 (34) (2021) 2102185.

[69] Y.K. Lee, K. Ahn, J. Cha, C. Zhou, H.S. Kim, G. Choi, S.I. Chae, J.H. Park, S.P. Cho, S.H. Park, Y.E. Sung, W.B. Lee, T. Hyeon, I. Chung, Enhancing P-type thermoelectric performances of polycrystalline SnSe via tuning phase transition temperature, J. Am. Chem. Soc. 139 (31) (2017) 10887–10896.

[70] Y.J. Fu, J.T. Xu, G.Q. Liu, X.J. Tan, Z. Liu, X. Wang, H.Z. Shao, H.C. Jiang, B. Liang, J. Jiang, Study on thermoelectric properties of polycrystalline SnSe by Ge doping, J. Electron. Mater. 46 (5) (2017) 3182–3186.

[71] T.R. Wei, C.F. Wu, X. Zhang, Q. Tan, L. Sun, Y. Pan, J.F. Li, Thermoelectric transport properties of pristine and Na-doped $SnSe_{(1-x)}Te_{(x)}$ polycrystals, Phys. Chem. Chem. Phys. 17 (44) (2015) 30102–30109.